

# The effect of peripheral contrast sensitivity functions on the performance of the foveated wavelet image quality index

Aliakbar Bozorgian, Marius Pedersen, and Jean-Baptiste Thomas; Norwegian University of Science and Technology, Norway

## Abstract

The Contrast Sensitivity Function (CSF) is an integral part of objective foveated image/video quality assessment metrics. In this paper, we investigate the effect of a new eccentricity-dependent CSF model on the performance of the foveated wavelet image quality index (FWQI). Our results do not show a considerable change in FWQI performance when it is evaluated against the LIVE-FBT-FCVR 2D dataset. We argue that the resolution of the head-mounted display used in the subjective experiment limits our ability to reveal the anticipated effect of the new CSF on FWQI performance.

## Introduction

Several mechanisms in the human visual system result in a non-uniform distribution of neural sampling elements throughout the retina [5]. It is well established that the sampling density is highest in a small region of the retina called the fovea and decreases as a function of angular distance (eccentricity). This change in the neural anatomy of the retina translates to a loss of contrast sensitivity and visual acuity in peripheral vision [18]. Foveated processing techniques exploit the decreased acuity in peripheral vision to improve graphical rendering and video transmission performance for displays with a wide field of view [15].

Omnidirectional videos are one of the main visual contents available for Head-Mounted Displays (HMDs). These videos provide a better sense of immersion than traditional videos due to the increased field of view and the possibility of exploring various viewing angles through head rotations. However, increased immersion comes at the expense of a significant increase in bandwidth consumption [10]. Foveated compression is a promising technique to alleviate the increasing demand for bandwidth in HMDs. The core idea of foveated compression is to track the location of the observer's gaze and deliver a high-fidelity image to foveal vision while at the same time exploiting the decreased sensitivity of peripheral vision for more rigorous compression without introducing visible artefacts [8]. As foveated algorithms mature, interest in foveated image and video quality assessment increases concurrently [10]. An objective foveated quality metric would be helpful in the evaluation and optimization of foveated processing algorithms, such as foveated compression. Furthermore, an efficient and differentiable metric could also be incorporated into the loss function of deep learning models [14]. Despite considerable progress in subjective and objective quality assessment of non-foveated content, foveated subjective and objective quality assessment are both still in their infancy.

LIVE-FBT-FCVR [10] is a recent dataset investigating the effect of VP9 compression artifacts in a foveated algorithm and provides subjective scores for 180 distorted videos generated from 10 reference 360-degree videos. Fovdots [14] is another recent foveated dataset of a synthetic foveated stimulus with varying luminance, contrast, and velocity rated by 35 observers.

The Foveal Mean Squared Error (FMSE) and Foveal Peak Signal to Noise Ratio (FPSNR) is based on the well-known MSE

and PSNR metrics to rate the quality of foveated content in curvilinear coordinates [12]. The Foveated Wavelet image Quality Index (FWQI) is a foveated image quality metric using an eccentricity-dependent Contrast Sensitivity Function (CSF) and wavelet analysis to estimate the quality of foveated images [19]. A recent video quality metric called fovVideoVDP takes into account the physical properties of the displays and implements psychophysical models to predict the quality of foveated videos in terms of just-objectionable difference units [14].

The main motivation in this paper is to study the effect of various eccentricity-dependent CSF models on the performance of the FWQI.

## Foveated wavelet image quality index

FWQI relies on wavelet analysis to measure the visual difference between a reference image and a distorted image based on the following expression [19]:

$$FWQI = \exp \left( - \left( \frac{1}{M} \sum_{n=1}^M (S_{fw}(\nu, \lambda_n, \theta_n, x_n) \times |c(x_n) - \tilde{c}(x_n)|)^2 \right)^{\frac{1}{2}} \right), \quad (1)$$

where  $M$  is the total number of wavelet coefficients, and  $S_{fw}$  is the foveated error sensitivity model in the wavelet domain that is a function of  $\nu$  as the viewing distance (expressed in image width),  $\lambda_n$  as the wavelet decomposition level,  $\theta_n$  as the orientation, and  $x_n$  as the position of the  $n$ th wavelet coefficient.  $c(x_n)$  is the value of the wavelet coefficient located at the coordinate  $x_n$  in the reference image, and  $\tilde{c}(x_n)$  is the value of the wavelet coefficient located at  $x_n$  in the distorted image.  $S_{fw}$  describes the sensitivity of an average observer to the difference in the wavelet coefficients of the reference image and distorted image and is described by  $S_{fw} = S_w^{\alpha_1} S_f^{\alpha_2}$ , where  $S_w$  is the error sensitivity for wavelet coefficients in sub-band  $(\lambda, \theta)$ ,  $S_f$  is the normalized foveation-based error sensitivity, and  $\alpha_1, \alpha_2$  are two parameters controlling the magnitude of  $S_w$  and  $S_f$ , respectively. Following the original implementation of FWQI we use  $\alpha_1 = 1$ , and  $\alpha_2 = 2.5$ .  $S_f$  is defined by the following expression:

$$S_f(\nu, f, x) = \begin{cases} \frac{CS(f, e(\nu, x))}{CS(f, e(\nu, 0))} & f \leq f_e(x, \nu) \\ 0 & f \geq f_e(x, \nu) \end{cases}, \quad (2)$$

where  $CS$  is an eccentricity-dependent CSF and  $f_e$  is effective cutoff frequency. Since the cutoff frequency could be limited by display resolution, we define effective cutoff frequency as  $f_e(x, \nu) = \min(f_c(e(x, \nu)), f_d(\nu))$  where  $f_c$  is the frequency at which  $CS = 1$  (cutoff frequency of CSF), and  $f_d$  is the highest frequency that can be represented on the display without aliasing. For displays that span a small field of view, the  $f_d$  in cycle per visual degree can be approximated as  $f_d, 0 = 0.5\pi / \left( 360 \arctan \left( \frac{0.5d_{width}}{r_n d_v} \right) \right)$ , where  $d_{width}$  is the display width

in meters,  $r_h$  is the horizontal resolution in pixels, and  $d_v$  is the viewing distance in meters [14]. However, in displays with a wide field of view, such as those of HMDs,  $f_d$  changes as a function of eccentricity based on the following formula:

$$f_d = f_{d,0} \frac{\tan\left(\frac{\pi e}{180} + 0.5f_{d,0}^{-1}\right) - \tan\left(\frac{\pi e}{180}\right)}{\tan\left(0.5f_{d,0}^{-1}\right)}. \quad (3)$$

The original implementation of FWQI relies on an empirical CSF proposed by Geisler [9] to compute the normalized contrast sensitivity as a function of eccentricity:

$$CS(f, e) = \frac{1}{CT_0} \exp\left(\alpha f \frac{e + e_2}{e_2}\right)^{-1}, \quad (4)$$

where  $e$  is eccentricity expressed in visual degrees,  $CT_0$  is the minimal contrast threshold,  $\alpha$  is the spatial frequency decay constant, and  $e_2$  is the half resolution eccentricity. These constants are fitted to the contrast threshold data published for small, briefly presented sinusoidal patches, which are the most relevant stimulus settings for predicting visibility. The Geisler CSF is simple and practical; however, it does not consider temporal frequency and does not capture the effect of luminance on contrast sensitivity. Extension to the temporal aspect is desirable while designing video quality assessment metrics and evaluating foveated videos. The ability to model contrast sensitivity as a function of luminance is also beneficial for high dynamic range displays.

## Barten contrast sensitivity function

Barten has proposed a physical model of CSF based on the assumption that contrast sensitivity is partially determined by the internal noise of the human visual system and partially by the Modulation Transfer Function (MTF) of the eye and lateral inhibition [2]. This model gives a thorough description of contrast sensitivity as a function of spatial frequency, stimulus field size, and has the possibility to be extended to the extra-foveal region and temporal domain. Barten's sensitivity function is defined as:

$$S(f, e, L, X, Y) = \frac{M_{opt}(f, e)}{2k} \sqrt{\frac{X(e)Y(e)T}{\Phi_{ph}(e) + \frac{\Phi_0(e)}{M_{lat}^2(f, e)}}}, \quad (5)$$

where  $f$  is the spatial frequency expressed in cycle per degree,  $e$  is eccentricity expressed in visual degrees,  $L$  is the luminance expressed in  $cd/m^2$ ,  $X$ ,  $Y$ ,  $T$  are the spatial and temporal dimension of the visual stimulus,  $k$  is a constant similar to the signal-to-noise ratio,  $\Phi_{ph}$  is photon noise,  $\Phi_0$  is neural noise,  $M_{lat}$  is the lateral inhibition MTF, and  $M_{opt}$  is the MTF of the eye.

In the original implementation of the Barten CSF, it is assumed that eccentricity parameter variations are mainly due to variations in the density of ganglion cells over the retina. Specifically, the MTF of the eye, which mediates the high-frequency portion of the CSF and consequently the cutoff frequencies, changes as a function of eccentricity by  $M_{opt}(f, e) = \exp(-2\pi\sigma(e)^2 f^2)$ , where  $\sigma(e)$  is the standard deviation of the line spread function describing the optical degradation stemmed from combined effect of the eye lens, the discrete structure of photoreceptors, stray light in the ocular media, and is modeled by  $\sigma(e) = \sqrt{\sigma_0^2(0) + \sigma_{ret}(e)^2 + (C_{abd})^2}$ , where  $\sigma(0)$  is a constant indicating the effect of ocular media in the fovea,  $\sigma_{ret}$  characterizes the effect of the retinal structure,  $C_{ab}$  is a constant controlling

the increase of  $\sigma$  with increasing pupil size, and  $d$  is the pupil diameter expressed in  $mm$ . The change in  $\sigma_{ret}$  with eccentricity is described by the following expression:

$$\sigma_{ret} = \frac{1}{\sqrt{7.2\sqrt{3}N_{M-on}}}, \quad (6)$$

where  $N_{M-on}$  is the density distribution of a subgroup of ganglion cells known as on-center parasol (M) cells. The typical values of the constants in Barten CSF are reported in [2].

Although Barten assumes that the achromatic CSF is solely supported by on-center parasol cells, there is a body of evidence from anatomical, and psychophysical studies supporting the theory that parasol and midget ganglion cells can contribute to the perception of luminance gratings [17]. In this view, the high-gain parasol (M) cells are well-tuned for the detection of low to medium spatial frequency luminance gratings [13, 17], while the condensed mosaic of midget cells provides the neural substrate for resolving high-frequency luminance patterns [6, 21]. In [3] the authors propose a modification to the Barten model to reflect on the composite contribution of parasol and midget cells to the achromatic CSF. Accordingly, the density of on-center parasol cells in Eq. 6 is changed to the density of the midget cells. Watson proposed the following expression for the total population of the midget cells: [20]:

$$d_{mf}(r, k) = 2d_c(0)\left(1 + \frac{r}{r_m}\right)^{-1} \left(a_k\left(1 + \frac{r}{r_{2,k}}\right)^{-2} + (1 - a_k)e^{-\frac{r}{r_{e,k}}}\right), \quad (7)$$

where  $r$  is eccentricity expressed in visual degrees,  $k$  is the index number of the corresponding meridian,  $d_c(0)$  is the density of cones in the fovea,  $r_m$  is the eccentricity at which midget cells make up half of the total ganglion cells,  $r_{2,k}$  is the eccentricity in the meridian  $k$  where density is decreased by a factor of four,  $a_k$  is a weighting factor, and  $r_{e,k}$  is the scale factor of the exponential in meridian  $k$ . The quantitative values of the constants are reported in [20]. The midget ganglion cells are composed of two subgroups called on- and off-center cells, and each is expected to form an individual array of sampling elements in the retina [6, 7]. It is anticipated that in the central retina the receptive fields of these two subgroups overlap, and hence, only 50 percent of the total population of the midget cells sample the cone mosaic [11]. Beyond 6 to 7 visual degrees, the receptive fields begin to diverge and the opportunity arises for on- and off-center cells to sample different locations of the cone mosaic, rendering the total population of the midget cells as the limiting array [16]. To model this effect, the following correction is applied to  $d_{mf}$ :

$$N_e = \left(1 - \left(\frac{0.5}{1 + \left(\frac{r}{r_t}\right)^4}\right)\right) d_{mf}, \quad (8)$$

where  $N_e$  is the effective density of the midget cells,  $r_t$  is the eccentricity at which the midget cells begin to collect input from more than a single cone. Finally, the  $N_e$  in Eq. 6 is substituted with  $N_{M-on}$  resulting in:

$$\sigma_{ret} = \frac{1}{\sqrt{7.2\sqrt{3}N_e}}. \quad (9)$$

Comparison with recently published contrast sensitivity data [4] reveals that the modified version of the Barten CSF results in more accurate estimates of the cutoff frequency compared to the original version [3]. Fig. 1A. demonstrates the variation in the cutoff frequency values of the Geisler, original, and

modified Barten CSFs as a function of eccentricity. The field size and luminance parameter in Barten-based CSFs are set to  $2^\circ$  and  $75 \frac{cd}{m^2}$ . These values are chosen to reflect the visibility conditions in a typical HMD. Although the Geisler and original Barten follow a similar trend, the modified Barten consistently results in higher cutoff frequencies through all eccentricities. The difference between cutoff frequency values of the original and modified Barten CSF is due to the different ganglion cell density functions used in Eqs. 6 and 9. If we define  $R_{mo}(e)$  as the ratio of the modified Barten's cutoff frequency values to the original Barten's cutoff frequency values, we can observe a significant increase of the ratio from the fovea to  $15^\circ$  of the visual field, where  $R_{mo}(e)$  reaches from 1 to 2.34 (Fig. 1B). Such a difference in the high-frequency region of the two models, as it is evident from the variation of  $R_{mo}$ , could influence the performance of a foveated metric that relies on contrast sensitivity and cutoff frequency values, such as FWQI.

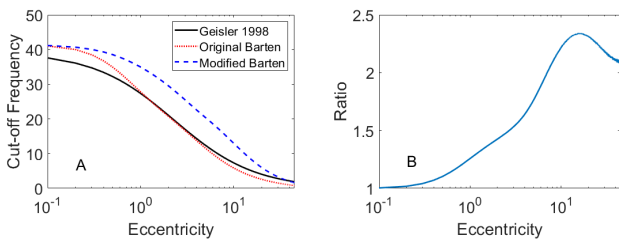


**Figure 1.** (A) cutoff frequency as a function of eccentricity; (B)  $R_{mo}$  as a function of eccentricity

### Barten contrast sensitivity function for foveated wavelet quality index

To investigate the potential effect of the modified Barten on the performance of the FWQI, we derive two additional versions of the FWQI named OB-FWQI and MB-FWQI, each using the contrast sensitivity and effective cutoff frequency ( $f_e$ ) values resulting from the original and modified Barten, respectively. Fig. 2 shows the error sensitivity for wavelet coefficients ( $S_w$ ) and the resulting normalized foveation-based error sensitivities ( $S_f$ ) from Geisler, original, and modified Barten CSF in a three-level decomposition square representation. The original and modified Barten behave similarly and both result in a more pronounced foveation effect compared to the Geisler CSF. However, in the Geisler CSF weights are distributed more evenly and sensitivity is diminished at a lower rate in higher eccentricities. Lower frequency levels, as shown in the upper left corner of the decomposition squares, are brighter for Geisler CSF compared to Barten CSFs. This behavior is associated with the low-pass nature of the Geisler CSF, where there is little room for attenuation of the sensitivity at lower frequencies as eccentricity increases.

### Evaluation

To evaluate the image quality metrics, we use the differential mean opinion scores (DMOS) reported in 2D LIVE-FBT-FCVR as ground truth data and follow the evaluation framework proposed by the authors of the dataset [10]. Despite dynamic foveation in the experiment, a fixed centered foveation is assumed for evaluation due to lack of access to eye-tracking data. Subsequently, the foveated experience of the observers who participated in the subjective experiment was simulated for objective metrics by generation of foveated viewports with a 90-degree field of view and three levels of compression. FWQI, OB-FWQI, and MB-FWQI scores were computed for 10 video contents  $\times$  18 distortions  $\times$  18 directions  $\times$  300 frames = 972000

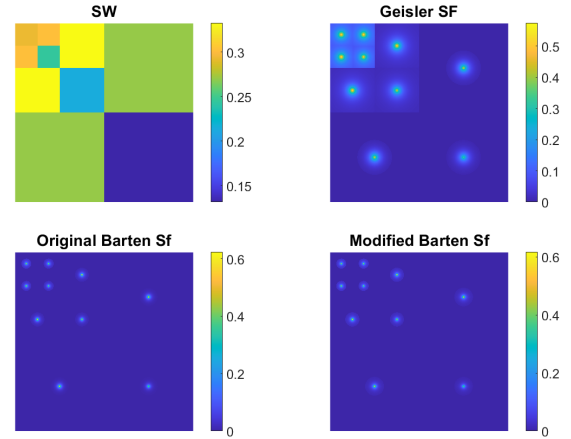


**Figure 2.** Top left: the error sensitivity for wavelet coefficients ( $S_w$ ) in subband  $(\lambda, \theta)$  derived from Watson's model. Top right: the normalized foveation-based error sensitivity derived from the Geisler CSF. Bottom left: the normalized foveation-based error sensitivity derived from the original Barten CSF. Bottom right: the normalized foveation-based error sensitivity derived from the modified Barten CSF.

viewports. Our analysis of the resulting scores shows that the standard deviation is small along different frames, but more pronounced along different directions (see Fig. 4). The lack of variation between frames might be explained by the stationary point of view in the 360-videos of the dataset. In fact, most of the temporal activity in the videos is originated by moving passengers or vehicles, which seem to be insignificant in terms of scale compared to fixed objects composing the scene. The variation among directions, highlights the need for inclusion of eye-tracking data and individual quality ratings in the subjective dataset since simple averaging of objective scores fails to address possible bias in the directions subjects chose to investigate. Standard deviation values for FWQI along different locations show a strong correlation with video content as it is evident from the distinct colors in the plot. However, in the case of MB-FWQI the correlation between standard deviation along directions and video content is diminished, instead there seems to be a negative correlation with DMOS. Finally, the scores are averaged among frames and directions to compare with the reported DMOS.

Three measures are implemented to evaluate the performance of the resulting objective metrics [1]: Pearson's linear correlation coefficient (PLCC), Spearman's rank-order correlation coefficient (SROCC), and outlier ratio. A four-parameter logistic regression was applied to the objective scores prior to computation of PLCC [1]:

$$Q(x) = \beta_2 + \frac{\beta_1 - \beta_2}{1 + \exp(-\frac{x - \beta_3}{|\beta_4|})}, \quad (10)$$

where the initial values for  $\beta_1$  to  $\beta_4$  are the maximum, minimum, mean, and standard deviation of the objective scores, respectively. Fig. 3 indicates the best-fitting logistic functions obtained by using the "nlinfit" function in MATLAB software. The relationship between objective and DMOS is demonstrated in the scatter plots of Fig. 3. Note that the shape of the fitted logistic function changes when the CSF is changed to Barten. This effect might be due to the difference in the type of sensitivity decay function implemented in the Geisler and Barten CSFs. In the case of the Geisler CSF, the loss of sensitivity as a function of eccentricity is characterized by an exponential decay function [19]. However, in the Barten CSF model the loss of sensitivity

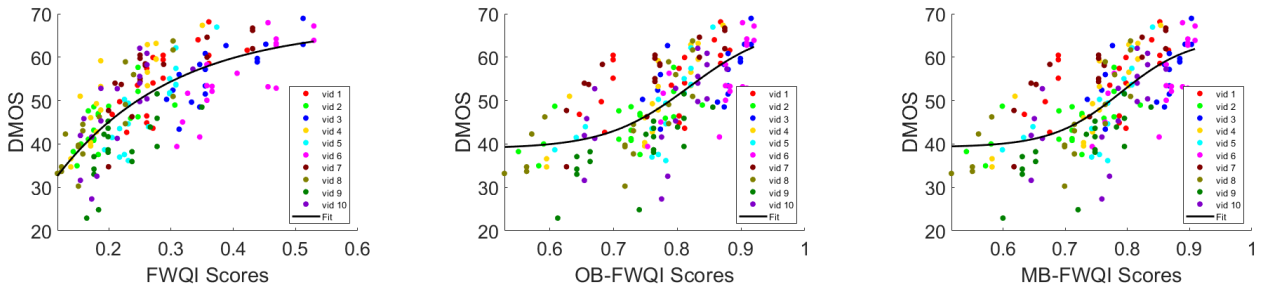


**Figure 3.** Scatter plots for FPSNR, OB-FPSNR, and MB-FPSNR versus DMOS were reported in the 2D LIVE-FBT-FCVR dataset. Scores belonging to a specific video content are given distinct colors. The black line shows the best-fitting logistic function on the objective scores.

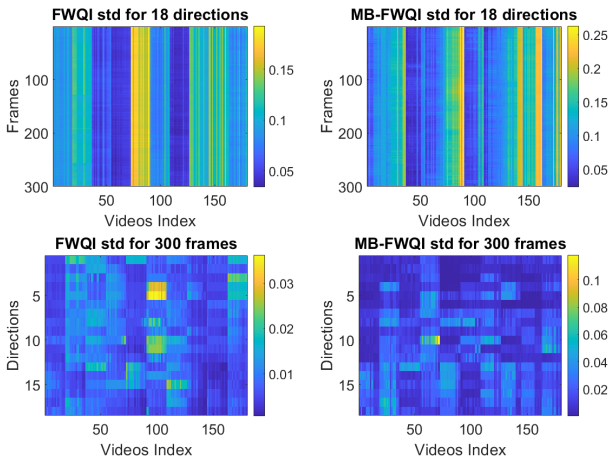


**Figure 4.** Top row: standard deviation for 18 directions in FWQI and MB-FWQI. Bottom row: standard deviation for 300 frames in FWQI and MB-FWQI. Plots for FWQI-OB are not provided because of the high similarity to FWQI-MB.

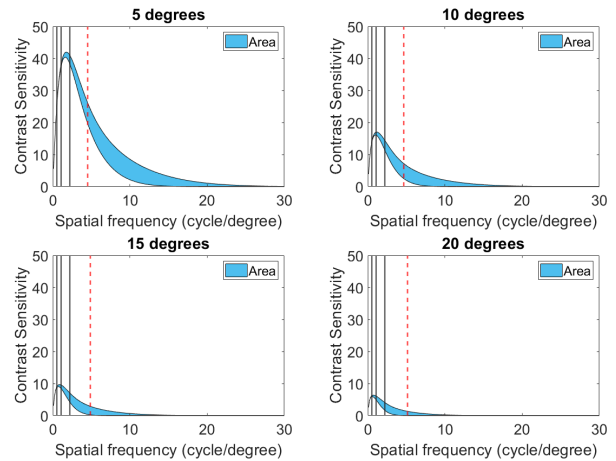


**Figure 5.** The difference between original and modified Barten CSF. The red dashed vertical line shows the highest frequency afforded by the HMD as a function of eccentricity. Grey lines demonstrate frequency of each wavelet decomposition level.

is mainly mediated by the neural noise term, which is characterized by the second power of eccentricity [2]. The resulting PLCC, SROCC, and outlier ratio are reported in Table 1. Of the three versions, the original implementation of the FWQI with the Geisler CSF results in the best overall performance. The resulting PLCC, SROCC, and outlier ratio scores are quite similar for OB-FWQI and MB-FWQI. The F-test does not show a significant difference in the performance of the metrics. We believe that the resolution of the HMD used in the LIVE-FBT-FCVR subjective experiment, and consequently resolution of the simulated viewports fed into the metric, limit our ability to reveal the difference between OB-FWQI and MB-FWQI metrics. To clarify this limitation, four plots are provided in Fig. 5, where the original and modified Barten CSF are plotted from 5 to 20 degrees of visual degrees. The area between the two CSF curves is marked with blue as an indicator of their difference. The red dashed line in the plots represents the highest representable frequency by the viewports (see Eq. 3) and three grey lines correspond to the frequencies of wavelet decomposition levels. One

could interpret the red dashed line as the highest limit for the frequencies presented to the observers during the subject experiment, and the grey lines as the frequencies investigated by the metric. In other words, none of the frequencies on the right side of the red dashed line were present in the subjective experiment, and only the frequencies on the left side were perceived by the observers. The resulting plots suggest that most of the difference between the two CSF curves (depicted by the blue area) lies on the right side of the red dashed-line. Therefore, the resolution of the HMD used in the LIVE-FBT-FCVR does not provide the required bandwidth to reveal the difference between the original and modified Barten.

**Table 1. Performance measures for objective metrics**

Objective metrics	PLCC	SROCC	Outlier Ratio
FWQI	0.7514	0.7419	0
OB-FWQI	0.6815	0.6939	0.0111
MB-FWQI	0.6875	0.6967	0.0111

## Conclusion

Two additional versions of the FWQI were derived through modification of the normalized sensitivity function. The resulting scores were then compared to DMOS reported in the 2D LIVE-FBT-FCVR dataset. The original implementation of the FWQI with Geisler CSF resulted in the best performance measures; however, F-test showed no significant difference in the performance of the three metrics. The performance measures for the OB-FWQI and MB-FWQI metrics are similar. Our study highlights the limitations of existing databases and the need to perform a foveated subjective quality assessment with a higher resolution HMD. Moreover, eye-tracking data and individual subjective quality ratings can be helpful for the elimination of fixed foveation assumption in evaluation framework.

## References

- [1] J. Antkowiak, T. D. F. Jamal Baina, F. V. Baroncini, N. Chateau, F. FranceTelecom, A. C. F. Pessoa, F. U. B. Stephanie Colonnese, I. L. Contin, J. Caviedes, and F. Philips. Final report from the video quality experts group on the validation of objective models of video quality assessment march 2000. 2000.
- [2] Barten and Peter G. *Contrast Sensivity of the Human Eye and its Effects on Image Quality*. 1999.
- [3] A. Bozorgian, M. Pedersen, and J. B. Thomas. Modification and evaluation of the peripheral contrast sensitivity function models. *Unpublished*, 2021.
- [4] M. Chwesiuk and R. Mantiuk. Measurements of contrast sensitivity for peripheral vision. In *Proceedings - SAP 2019: ACM Conference on Applied Perception*, 2019.
- [5] L. K. Cormack. Computational Models of Early Human Vision. In *Handbook of Image and Video Processing*, pages 325–345. Academic Press, 1 2005.
- [6] D. M. Dacey. The mosaic of midget ganglion cells in the human retina. *Journal of Neuroscience*, 13(12):5334–5355, 1993.
- [7] E. V. Famiglietti and H. Kolb. Structural basis for ON- and OFF-center responses in retinal ganglion cells. *Science*, 194(4261):193–195, 10 1976.
- [8] A. Floren and A. C. Bovik. Foveated Image and Video Processing and Search. volume 4, pages 349–401. Elsevier, 1 2014.
- [9] W. S. Geisler and J. S. Perry. Real-time foveated multiresolution system for low-bandwidth video communication. *Human Vision and Electronic Imaging III*, 3299(July 1998):294–305, 1998.
- [10] Y. Jin, M. Chen, T. Goodall, A. Patney, and A. C. Bovik. Subjective and Objective Quality Assessment of 2D and 3D Foveated Video Compression in Virtual Reality. *IEEE Transactions on Image Processing*, 30:5905–5919, 6 2021.
- [11] H. Kolb and L. Dekorver. Midget ganglion cells of the parafovea of the human retina: A Study by electron microscopy and serial section reconstructions. *Journal of Comparative Neurology*, 303(4):617–636, 1991.
- [12] S. Lee, M. S. Pattichis, and A. C. Bovik. Foveated video quality assessment. *IEEE Transactions on Multimedia*, 4(1):129–132, 3 2002.
- [13] P. Lennie, J. Pokorny, and V. C. Smith. Luminance. *Journal of the Optical Society of America A*, 10(6):1283, 1993.
- [14] R. K. Mantiuk, G. Denes, A. Chapiro, A. Kaplanyan, G. Rufo, R. Bachy, T. Lian, and A. Patney. FovVideoVDP: A visible difference predictor for wide field-of-view video. *ACM Transactions on Graphics*, 40(4), 7 2021.
- [15] A. Patney, J. Kim, M. Salvi, A. Kaplanyan, C. Wyman, N. Bentley, A. Lefohn, and D. Luebke. Perceptually-based foveated virtual reality. In *ACM SIGGRAPH 2016 Emerging Technologies, SIGGRAPH 2016*, pages 1–2, New York, New York, USA, 7 2016. Association for Computing Machinery, Inc.
- [16] S. J. Schein. Anatomy of macaque fovea and spatial densities of neurons in foveal representation. *Journal of Comparative Neurology*, 269(4):479–505, 1988.
- [17] R. Shapley. Visual sensitivity and parallel retinocortical channels. *Annual Review of Psychology*, 41(1):635–658, 11 1990.
- [18] L. N. Thibos, D. L. Still, and A. Bradley. Characterization of spatial aliasing and contrast sensitivity in peripheral vision. *Vision Research*, 36(2):249–258, 1996.
- [19] Z. Wang, A. C. Bovik, L. Lu, and J. L. Kouloheris. Foveated Wavelet Image Quality Index. *Applications of Digital Image Processing XXIV*, 4472:42–52, 2001.
- [20] A. B. Watson. A formula for human retinal ganglion cell receptive field density as a function of visual field location. *Journal of Vision*, 14(7):1–17, 2014.
- [21] M. O. Wilkinson, R. S. Anderson, A. Bradley, and L. N. Thibos. Neural bandwidth of veridical perception across the visual field. *Journal of Vision*, 16(2):1–17, 1 2016.

## Author Biography

*Aliakbar Bozorgian received his B.Sc. and M.Sc. in polymer engineering and color science from Amirkabir University of Technology in 2017 and 2020, respectively. Since then he has been enrolled in the Ph.D. programme in the department of computer science at the Norwegian University of Science and Technology. His research interests include visual perception, image quality assessment and virtual reality.*

*Marius Pedersen received his BsC in Computer Engineering in 2006, and MIt in Media Technology in 2007, both from Gjøvik University College, Norway. He completed a PhD program in color imaging in 2011 from the University of Oslo, Norway, sponsored by Océ. He is professor at the Department of Computer Science at NTNU in Gjøvik, Norway. He is also the director of the Norwegian Colour and Visual Computing Laboratory (Colourlab). His work is centered on subjective and objective image quality.*

*Jean Baptiste THOMAS received his Bachelor in Applied Physics (2004) and his Master in Optics, Image and Vision (2006) from Université Jean Monnet in France. He received his PhD from Université de Bourgogne in 2009. Since 2010, he is Associate Professor at the Université de Bourgogne. Between 2016 and 2019 he was in a sabbatical at NTNU as Researcher, and from 2019 as Associate Professor. He has worked extensively on the development of spectral imaging systems through Spectral Filter Arrays technology. Since 2016 he has worked in understanding material appearance and its measure by using imaging systems. More information at <http://jbsthomas.org/>*